JOURNAL OF SPACECRAFT AND ROCKETS
Vol. 42, No. 2, March–April 2005

Navier–Stokes Computations for a Spinning Projectile from Subsonic to Supersonic Speeds

S. I. Silton*
U.S. Army Research Laboratory, Aberdeen Proving Ground, Maryland 21005

A computational study has been undertaken to predict the static-aerodynamic, Magnus-moment, and roll-damping coefficients of a standard spinning projectile using a single, modern, unstructured Navier–Stokes flow solver. Numerical results without engraving and semi-empirical results have been obtained for a wide range of Mach numbers to include subsonic, transonic, and supersonic flight regimes. Effects of 0-, 2-, and 5-deg angles of attack have been investigated. Flowfield characteristics of each flight regime are briefly explored. A comparison of coefficients calculated from the computational fluid dynamics results are made to both experimental range data as well as semi-empirical aeroprediction code results with some success. Good predictive capabilities are found for the static aerodynamic coefficients throughout all of the flight regimes. Discrepancies arise between the computational results and the experimental results for the Magnus moment and roll-damping coefficients due in part to the lack of engraving on the computational model.

Nomenclature

C_D = drag coefficient, $D/\frac{1}{2}\rho V_\infty^2 S$
C_{D0} = zero-yaw drag coefficient
$C_{L\alpha}$ = lift-force-coefficient derivative, $L/\frac{1}{2}\rho V_\infty^2 S\delta$
C_{lp} = roll-damping coefficient (roll-rate derivative), roll damping moment$/\frac{1}{2}\rho V_\infty^2 Sd(p_s d/V_\infty)$
$C_{\mathrm{Mp}\alpha}$ = Magnus moment coefficient derivative, Magnus moment$/\frac{1}{2}\rho V_\infty^2 Sd(p_s d/V_\infty)\delta$
$C_{M\alpha}$ = overturning moment coefficient derivative, static moment$/\frac{1}{2}\rho V_\infty^2 Sd\delta$
$C_{\mathrm{Np}\alpha}$ = Magnus force coefficient derivative, Magnus force$/\frac{1}{2}\rho V_\infty^2 Sd(p_s d/V_\infty)\delta$
C_p = pressure coefficient, $(p - p_\infty)/\frac{1}{2}\rho V_\infty^2$
D = drag force, N
d = reference diameter, m
L = lift force, N
M = Mach number
p = pressure, N/m^2
p_s = roll rate, rad/s
S = reference area, $\pi d^2/4$
V_∞ = freestream velocity, m/s
y^+ = normal viscous sublayer spacing
α = angle of attack, deg
δ = $\sin\alpha$
δ_e^2 = effective square yaw
ρ = air density, kg/m^3

Introduction

COMPUTATIONAL fluid dynamics (CFD) has been used for many years to determine the aerodynamic coefficients of smooth, spinning projectiles.[1–3] These early numerical studies have produced favorable results when compared to data obtained from smooth body wind-tunnel tests. However, many of the smaller-caliber (cal.) Army projectiles are slender, spinning bodies that become engraved when fired from a rifled barrel. CFD models are often constructed without engraving for ease of grid generation and reduction of computation time. The lack of engraving on the models likely causes discrepancies in the computed aerodynamic coefficients. Limited experimental research[4,5] has shown that the presence of rifling grooves does, in fact, affect the aerodynamic coefficients. As much research is now conducted using CFD, it is important to understand the limitations of what is being modeled.

The 0.50-cal. projectile chosen for this study has been in use for almost 60 years. Although a limited amount of aerodynamic data was collected during the projectile's development and testing,[6] a relatively large amount of aerodynamic data has been obtained over the years. Most of the data have been collected within the past 15 years at the U.S. Army Ballistic Research Laboratory's Free Flight Aerodynamics Range.[7] Parabolized Navier–Stokes numerical aeroballistic data have also been obtained for a similarly shaped 0.50-cal. training round with fairly good results.[8]

The present study was undertaken in order to verify the ability of one CFD package to predict the aeroballistic data for a spinning projectile over the entire flight regime and to determine where the deficiencies of modeling an engraved projectile as smooth body lie. This particular CFD software has been previously used to calculate the flowfield and resulting aeroballistic data on nonspinning projectiles,[9] but had not yet been benchmarked for spinning projectiles with the associated forces and moments. Prior to using this software to determine aeroballistic data for new spinning projectile designs, the software must be verified against existing data and methods, such as a semi-empirical code, to determine its accuracy. A similar study should be completed prior to any CFD package being used to predict aeroballistic coefficients.

Model Geometry and Numerical Grid

Numerical Geometry and Grid

The computational model is a 0.50-cal. (1 cal. = 12.95 mm) projectile, 4.46 cal. in length, with a 0.16-cal.-long, 0.02-cal.-deep groove, and a 9-deg filleted boattail[7] (Fig. 1). A center of gravity location of 2.68 cal. (34.706 mm) from the nose tip was utilized.

All grids used in this study were three-dimensional hexahedral meshes created using GRIDGEN ver. 13[10] (Pointwise). The grid is created in a multiblock format in order to allow for a better quality mesh and then written in an unstructured format. While GRIDGEN ver. 13 does not output meshes in CFD++ format, Fluent ver. 5[11] output format is available, which CFD++ is able to import.

Three separate meshes were constructed over the course of this study: one for the subsonic, transonic, and low supersonic cases and two for the supersonic cases. Two different computational grids were

Presented as Paper 2003-3936 at the AIAA 21st Applied Aerodynamics Conference, Orlando, FL, 23–26 June 2003; received 28 July 2003; revision received 30 April 2004; accepted for publication 30 April 2004.

*Aerospace Engineer, Weapons and Materials Research Directorate, Ballistics and Weapons Concepts Division, Aerodynamics Branch, AMSRD-ARL-WM-BC; ssilton@arl.army.mil. Member AIAA.

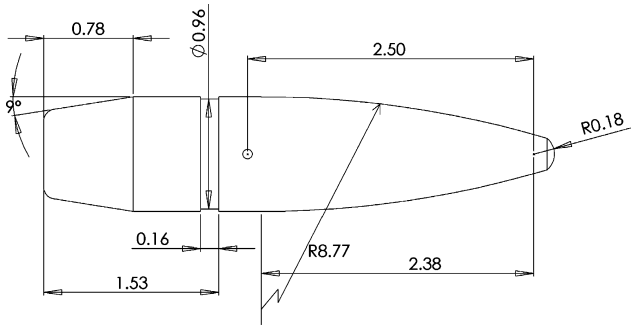

a)

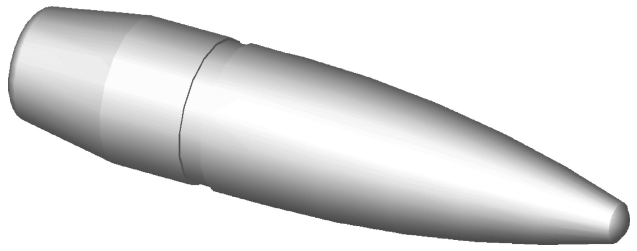

b)

Fig. 1 The 0.50-cal. projectile used for computational model: a) dimensional sketch, with all dimensions in calibers, and b) three-dimensional model.

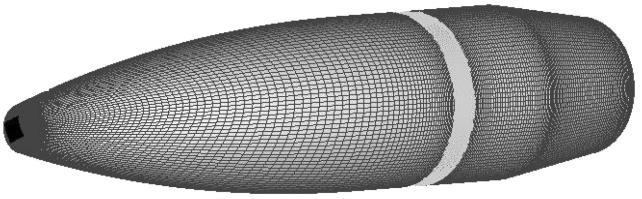

Fig. 2 Representative surface grid where sections are indicated by different colors.

created for the supersonic cases in order to verify grid independence. In each case, the far-field boundary was created so that it would not interfere with the flowfield in all of the regimes investigated (subsonic, transonic, and supersonic).

The mesh is composed of 10 structured blocks. The surface grid (Fig. 2) was generated first and consists of four sections: two small squares (black) projected on the nose and base to eliminate singularities on the symmetry axis, the groove (light gray), and the remainder of the body (dark gray). After constructing a companion far-field grid, radial planes were constructed between these two surface grids in order to create three-dimensional blocks. Two of these blocks are small rectangular blocks beginning at the small projected squares on the nose and base of the body and extending to the outer boundary (each 30×30 cells on the body), with the axial dimension equal to the radial dimension of the remaining flowfield. The rest of the body is divided into quadrants based on the corners of the surface squares, with the groove blocked separately. Each quadrant of the groove contains 30 radial cells, 30 circumferential cells, and 18 axial cells, while each quadrant for the remainder of the flowfield varied with the position of the far-field boundary. To accurately capture the flow in the turbulent boundary layer, the first radial surface spacing was always set to 1.07 μm.

For both supersonic grids, the outflow boundary was two body lengths behind the base of the model, the inflow boundary was just over one body length in front of the model, and the circumferential boundary was also just over one body length away from the model (Fig. 3). The medium-resolution grid contained 30 circumferential cells, 80 radial cells (away from the body), and 279 cells along the body surface and far-field boundary in one quadrant (2,737,658 cells total) while the fine-resolution grid contained 30 circumferential cells, 150 radial cells, and 296 cells along the body surface in one

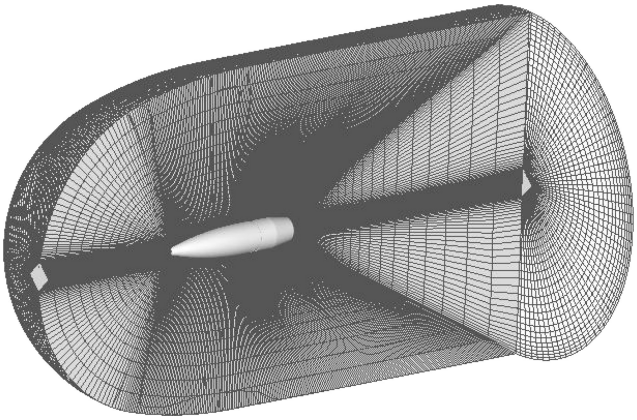

Fig. 3 Grid used for medium-resolution supersonic CFD solutions.

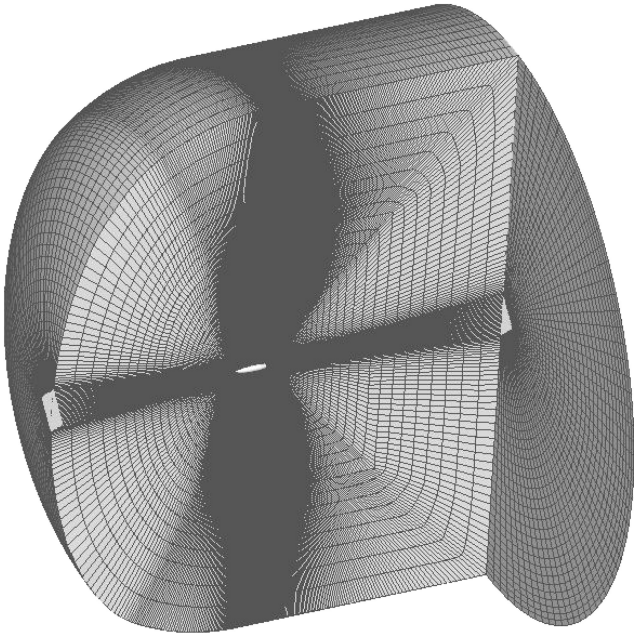

Fig. 4 Grid used for subsonic, transonic, and low supersonic CFD solutions.

quadrant (5,413,314 cells total). The additional radial cells were added near the surface so that the boundary-layer cell thickness grew more slowly. The additional axial cells were added in the nose and base regions. The greater number of cells in the radial and axial directions for the finer grid allowed finer details of the flowfield to be studied.

The mesh created for the subsonic, transonic, and low supersonic cases was similar in structure to that created for the supersonic case. The far-field boundary was moved further away from the projectile body (Fig. 4) to accommodate the weaker shocks, expansions, and longer recovery distances of flowfield features. The new inflow boundary was located just under three body lengths away, the outflow boundary eight body lengths away, and the circumferential boundary almost 10 body lengths away. While the circumferential dimension remained constant at 30 cells in one quadrant, the radial dimension was increased to 109 cells, and the axial dimension to 289 cells in order to accommodate the new position of the far-field boundary. The additional axial cells were added on the nose and the base of the projectile. The complete mesh consisted of 4,041,120 cells.

Semi-Empirical Geometry

The assumptions within the semi-empirical solution all pertained to the afterbody geometry because of limitations of the software. First, the groove was eliminated, as the software could not handle a decrease in body radius followed by a subsequent increase.

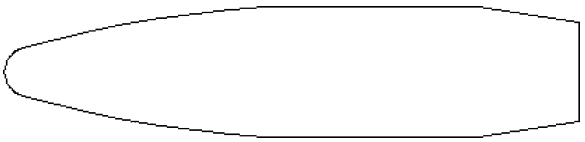

Fig. 5 Geometry utilized in semi-empirical method (no groove, straight boattail).

Additionally, the filleted boattail was eliminated and replace with a standard 9-deg angle boattail. These modifications to the geometry produced a model with the cross section in Fig. 5 and allowed for a solution to be calculated. The center of gravity for the semi-empirical solution was assumed to be that of the experimental model with the groove and filleted boattail. During geometry definition, one must also specify the model (boundary-layer) type. The typical flight option was utilized for consistency with the computational model.

Solution Technique

Numerical Techniques

CFD++[12] (Metacomp Technologies) ver. 3.5 was utilized for this study. CFD++ solves the Reynolds-averaged Navier–Stokes equations with pointwise turbulence models. The equations are solved within a finite volume framework using an unstructured grid topology. Spatial discretization is accomplished using the cell face normal at the cell face centroid, which is obtained by reconstructing the cell centroid values. Both implicit and explicit time-integration schemes are available. For the present study, the point-implicit integration scheme was used to solve the steady-state simulation. Ramping of the Courant number allowed for quicker solution convergence as the flow progressed towards solution, and larger time steps had less effect on the solution. The data to which the CFD is compared were determined from the firing of actual test projectiles. These projectiles are not necessarily smooth and could cause the boundary layer to trip very near the nose tip. Unfortunately, there is no way to accurately determine this from the available data. However, for the study presented herein, the boundary layer is assumed to be fully turbulent. The realizable k–ε turbulence model,[13] available within CFD++, was utilized.

The flowfield domain is initialized using freestream conditions. The far-field boundary (including inflow and outflow boundaries) utilized the characteristic-based boundary condition. This allows the software to determine the conditions (inflow, subsonic outflow, or supersonic outflow) at the boundary and either explicitly set the boundary conditions to freestream conditions (inflow, subsonic outflow) or extrapolates as necessary (supersonic outflow). Absorbing layers were utilized at the far-field boundary for some Mach numbers within the transonic regime (Mach 0.85 to 0.98) in order to prevent wave reflections from the boundaries and encourage a converged solution. Freestream pressure and temperature are set to 101,325 Pa and 288 K, respectively. The software then uses the perfect gas assumption to calculate density. Velocity is varied between Mach 0.60 and 2.7. For the projectile body, the boundary condition is set to be a no-slip, isothermal wall (at 288 K) that is rotating about the x axis. The projectile rotates at a speed corresponding to the rifling twist rate of the experiments[7] of one turn in 38.1 cm.

The simulations were performed in parallel using the double precision solver on either an IBM SMP P3 machine (SP3) with Power3 processors or an IBM SMP P4 machine (SP4) with Power4 processors. The number of processors used to obtain the solutions depended on the grid that was being used. The transonic grid was used to obtain the CFD solution for all Mach numbers below 1.5. The solution for Mach 1.5 was obtained on both the transonic and supersonic grid with less than a 1.5% difference in the calculated coefficients. The transonic grid was run on 32 processors as was the fine supersonic grid while the medium-resolution grid was run on 20 processors. The calculations took about 12 h of CPU time on the SP4 and 38 h on the SP3 for the solutions obtained on the transonic grid. Convergence was typically achieve in about 2000 iterations, depending on the Mach number. The solution was considered converged when the flow residual had either reduced at least three orders of magnitude and were no longer changing or had reduced seven orders of magnitude. The aerodynamic coefficients also needed to be changing, on average, less than 1% during the final 100 iterations.

Semi-Empirical Method

The semi-empirical solution was obtained using the Aeroprediction code AP02 (Ref. 14). This code was originally developed by the U.S. Navy in 1972 as a code to predict the aerodynamic performance of spin-stabilized projectiles. AP02 combines a large database of experimental results and well-verified numerical results with theoretical methods in order to obtain aerodynamic coefficients and dynamic derivatives. The theoretical methods include second-order van Dyke and second-order shock expansion theory as well as thin wing theory and slender body assumptions. It allows coefficients to be obtained in a relatively short period of time within engineering accuracy, as no grid is needed.

Results and Discussion

A number of numerical cases were studied in order to cover the range of experimental data available. The Mach numbers investigated encompass three projectile flight regimes: 1) subsonic, 2) transonic, and 3) supersonic. The Mach numbers and corresponding roll rates investigated can be found in Table 1. The small delta between numbers between Mach 0.85 and 1.10 is due to the rapidly changing flow characteristics in the transonic regime. A CFD calculation was completed for each Mach number at 0-, 2-, and 5-deg angles of attack.

For the CFD, C_{D0} and C_{lp} were obtained directly from the $\alpha = 0$ deg calculation. Solutions for the semi-empirical code were obtained at $\alpha = 2$ deg for the static coefficients and $\alpha = 5$ deg for the dynamic derivatives. All coefficient results are presented in the convention put forth by Murphy.[15]

Grid-Resolution Study

A grid-resolution study was conducted for the supersonic, Mach 2.70 case at both 0- and 2-deg angles of attack. This study was completed with CFD++ ver. 3.4. The Mach 2.70 case has the thinnest boundary layers and the most distinct flow physics for comparison. The solutions on the 2.7-million-cell (medium) and 5.4-million-cell (fine) grids were compared for differences in flow physics and aerodynamics coefficients, as well as for agreement with experimental data. After an initially high y^+ value at the nose tip, a peak y^+ value of approximately 1.75 is observed at the front of the ogive and steadily decreases along the length of the body (Fig. 6). The exception to this is at the groove, where there is a spike in the y^+ value (not shown in Fig. 6).

At $\alpha = 0$ deg, the medium and fine grids gave nearly identical results (less than 1%) for C_D and C_{lp} (Table 2). All other coefficients had values very near zero as expected. The discrepancy between the experimental and numerical results for C_{lp} is believed to be caused by the lack of engraving on the numerical modeling, as the numerical

Table 1 Mach numbers and resulting roll rates utilized in CFD calculations

Mach no.	Roll rate, rad/s
0.60	3,366.9
0.70	3,927.9
0.85	4,768.5
0.90	5,050.3
0.94	5,274.7
0.98	5,499.2
1.05	5,892.0
1.10	6,172.5
1.25	7,014.2
1.50	8,417.0
2.00	11,222.8
2.70	15,150.6

Table 2 Grid-resolution study at Mach 2.7, $\alpha = 0$ deg

Methodology	C_D	C_{lp}
Medium grid	0.2935	−0.00768
Fine grid	0.2964	−0.00766
M33 experiment[7]	0.279	−0.011

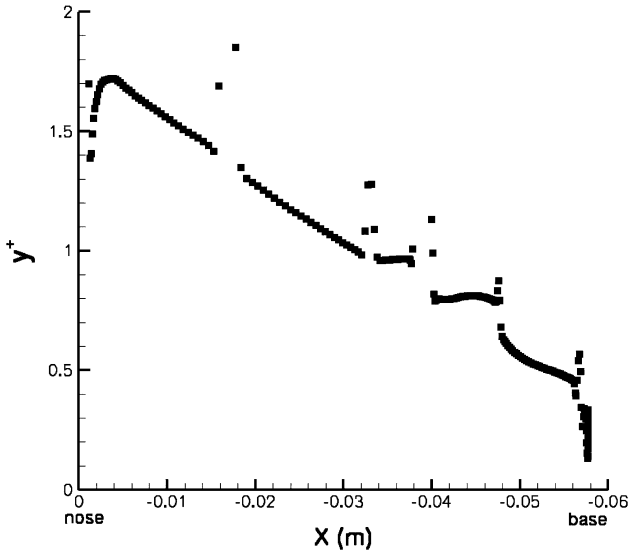

Fig. 6 The y^+ variation axially along body. Nose is at $x = 0$ and groove at $x = -0.039$.

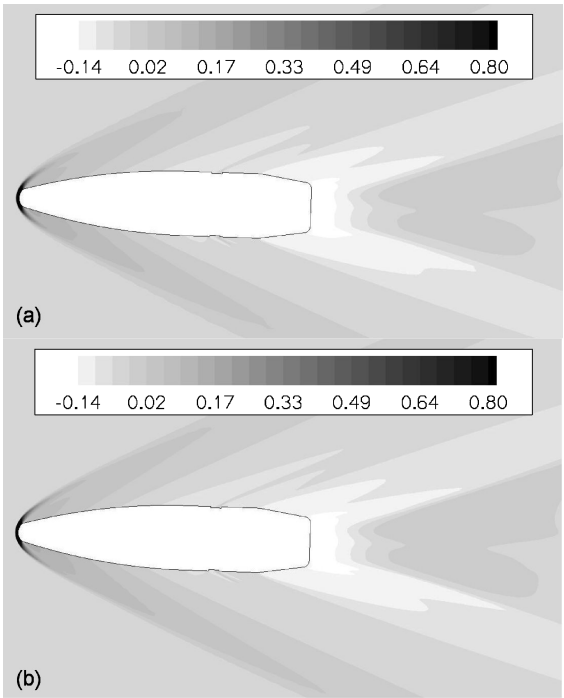

Fig. 7 Pressure coefficient contour comparison between a) medium- and b) fine-resolution grids in the vertical symmetry plane at Mach 2.7, $\alpha = 2$ deg.

results seem to agree with the data presented by Guidos and Chung.[8] The flowfields on both grids were very similar.

When the angle of attack is increased to 2 deg in the vertical symmetry plane, the flow becomes more complicated as it is no longer axisymmetric. The flow around the body was nearly identical between the two grids (Figs. 7 and 8), although some of the flow features were slightly better defined on the fine grid. Most of the aerodynamic coefficients, including $C_{\mathrm{Mp}\alpha}$, differed by no more than 0.5% (Table 3). Only C_D and $C_{\mathrm{Np}\alpha}$, differed to a greater extent. C_D

Table 3 Grid resolution study at Mach 2.7, $\alpha = 2$ deg; experimental data at closest data point

Methodology	C_D	$C_{L\alpha}$	$C_{\mathrm{Np}\alpha}$	$C_{\mathrm{Mp}\alpha}$	$C_{M\alpha}$	C_{lp}
Medium grid	0.3027	2.23	0.0637	0.21	2.79	−0.00767
Fine grid	0.3062	2.23	0.0710	0.21	2.80	−0.00765
M33 experiment[7]	0.2813	2.21	——	0.15	3.01	−0.011
M8 experiment[7]	0.2991	2.42	——	0.24	2.85	−0.011

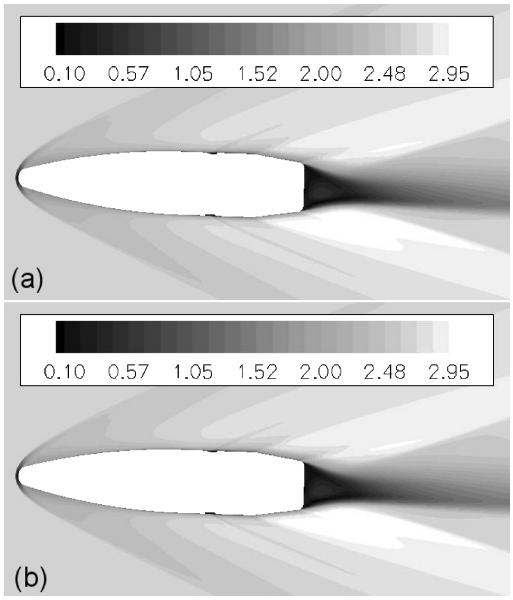

Fig. 8 Mach number contour comparison between a) medium- and b) fine-resolution grids in the vertical symmetry plane at Mach 2.7, $\alpha = 2$ deg.

increased slightly more than 1% between the medium and fine grids, and $C_{\mathrm{Np}\alpha}$ increased by ~10%. As the Magnus force is so small, this is not unexpected. For the coefficients compared in this study (i.e., not $C_{\mathrm{Np}\alpha}$ as there is no experimental data), the CFD error is expected to be no more than approximately 1%.

Both sets of numerical results agreed quite well with the experimental data, with the exception of C_{lp}. The discrepancy is again attributed to modeling a smooth projectile rather than an engraved projectile. As the results are nearly identical using either grid, it was not worth the nearly doubled computational time required in order to obtain a converged solution on the fine grid as compared to that for the medium grid. As such, the medium grid was utilized for the remainder of the supersonic cases, and comparable grids were used for the transonic and subsonic cases.

Flowfield Visualization

Within each flow regime investigated, there are certain flow features that one would expect to see. The flowfields for three Mach number cases, one in each flow regime, are shown in Figs. 9 and 10. Figure 9 shows a planar cut of the Mach number and C_p contours for $\alpha = 0$ deg. As expected the flow is axisymmetric for all Mach numbers at $\alpha = 0$ deg. The subsonic, $M = 0.70$ case (Figs. 9a and 9b) clearly shows that no shocks are present anywhere along the projectile indicating that the flow does indeed remain subsonic along the entire length of the projectile. The standard stagnation region and associated velocity decrease are present upstream of the nose tip as the flow anticipates the presence of the projectile. Note that the flow in the groove is nearly stagnant. The flow then expands and separates as it passes the boattail creating a low-velocity, nominal-pressure region of base flow. The transonic, $M = 0.98$ case (Figs. 9c and 9d) shows the subsonic stagnation region and associated velocity decrease upstream of the nose tip. One can also see the the expansions fans and recompression shocks at the ogive-body transition, the groove, the boattail-body transition, and the projectile

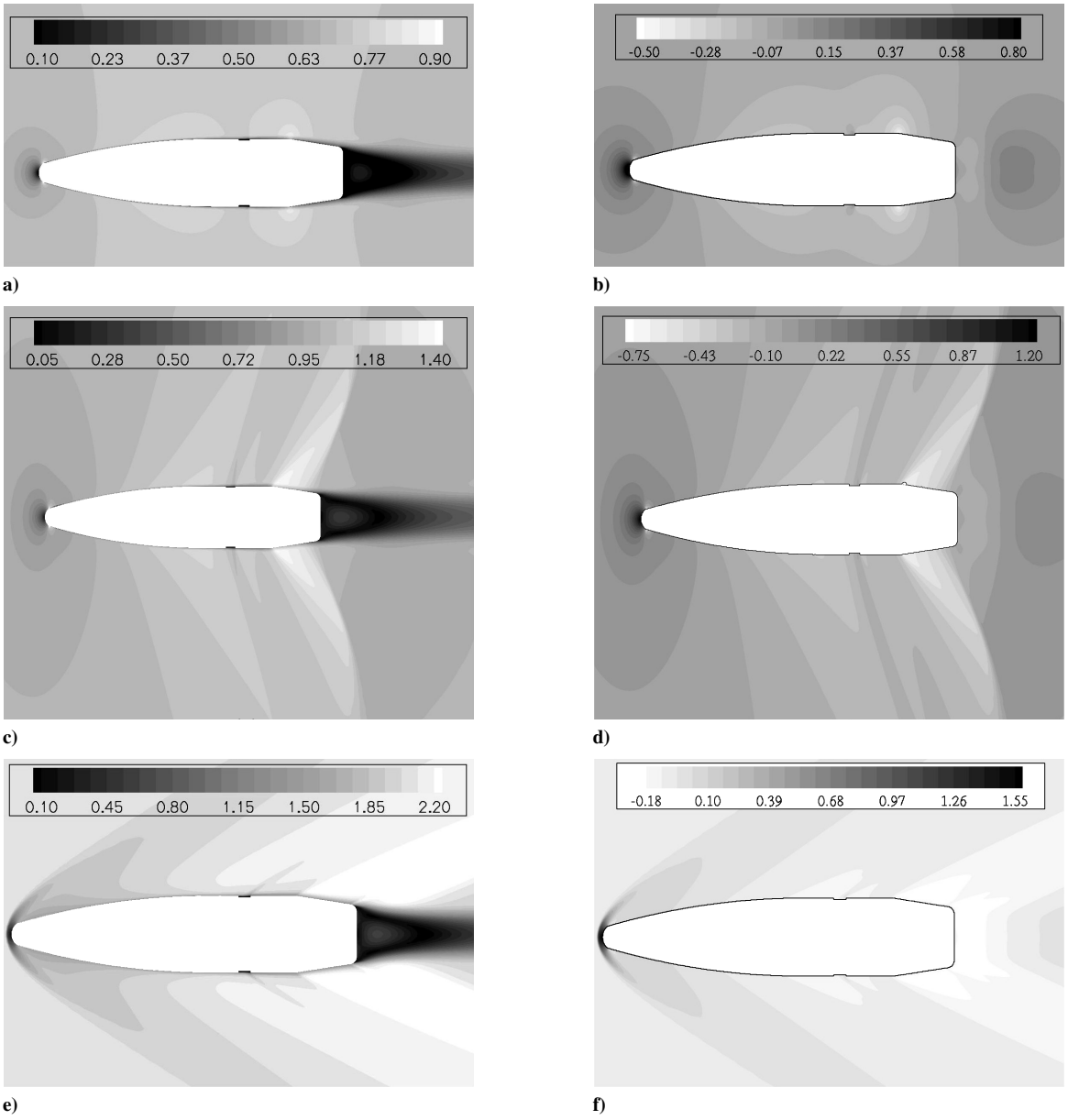

Fig. 9 Planar cut on symmetry plane of Mach number and C_p contours for a,b) $M = 0.70$, c,d) $M = 0.98$, and e,f) $M = 2.0$ at $\alpha = 0$ deg.

base. Note the large expanse of the flow recovery distance typical of a transonic flow. At Mach 2.0 (Figs. 9e and 9f) an oblique bow shock exists, and the expansion fans and recompression shocks along the projectile have become more well defined.

At angles of attack other than 0 deg, the flow becomes asymmetrical. Because of the rotation of the projectile, asymmetries occur in both the pitch and yaw planes even though the initial flow over the projectile is asymmetric in only the pitch plane. The small asymmetries in the yaw plane accounts for the nonzero, though extremely small, side (Magnus) force and Magnus moment. As the asymmetries are much more apparent in the pitch plane, Fig. 10 shows Mach-number and C_p contours on the vertical symmetry plane at $\alpha = 5$ deg. Note the differences in pressure contours in the base flow region between the different Mach numbers.

Data Comparison

A data comparison of the AP02, CFD, and experimental results is presented for all static aerodynamic coefficients C_{lp} and $C_{\mathrm{M}p\alpha}$. The experimental data used in this comparison were obtained in the U.S. Army Research Laboratory Aerodynamics Range.[7] Although experimental data were obtained for three different 0.50-cal. rounds, only the data for the M33 ball projectile (M33 experiment) and the M8 API projectile (M8 experiment) were used. The data from the third round were not utilized as it contained a tracer, which can change the aerodynamic characteristics. Each of these projectiles have the same nominal external dimensions (Fig. 1) and differ only in surface details, such as rolled versus machined cannelures.[7]

Plotted experimental data were limited to 1 deg $< \alpha \leq 5$ deg. Smaller yaw angles ($\alpha < 1$ deg) were unavailable, and although larger yaw angles ($\alpha > 5$ deg) were available, CFD results were obtained for a maximum angle of 5 deg (Ref. 8). Although larger angles were present in the experimental data, nonlinearities are often a factor in large yaw-angle analysis and cannot be accurately compared to the smaller yaw-angle data for the static aerodynamic coefficients. The error levels associated with experimentally obtained range data are listed in Table 4 (Ref. 16). No comparison to pitch damping moment is made in this study.

A comparison of zero-yaw drag C_{D0} was completed first. As expected, good agreement was obtained between the computational, semi-empirical, and experimental results (Fig. 11). Although the numerical solution overpredicts the experimental C_{D0} results slightly, the semi-empirical solution underpredicts them. The overprediction in the CFD is likely caused by a fully turbulent boundary layer

being assumed and the free flight flow either being laminar or, more likely, transitioning at some point along the projectile, rather than fully turbulent.

C_D was also compared (Fig. 12). Good agreement occurs at both $\alpha = 0$ and 2 deg. C_D appeared to be a bit high at $\alpha = 5$ deg. The agreement of the semi-empirical solution ($\alpha = 2$ deg) to the $\alpha = 2$ deg CFD solution and the range data was also quite good. The agreement between the predicted (both CFD and semi-empirical) and experimental data at $\alpha = 2$ deg reflects the small angles of attack used from the experimental data. Figure 12 clearly shows the

Table 4 Expected aerodynamic coefficient aeroballistic range error[16]

Aerodynamic coefficient	Percent error
Axial force	1–2
Normal force	5–10
Magnus force	25
Pitching moment	0–3
Pitch damping moment	10–20
Magnus moment	10–20
Roll damping moment	10

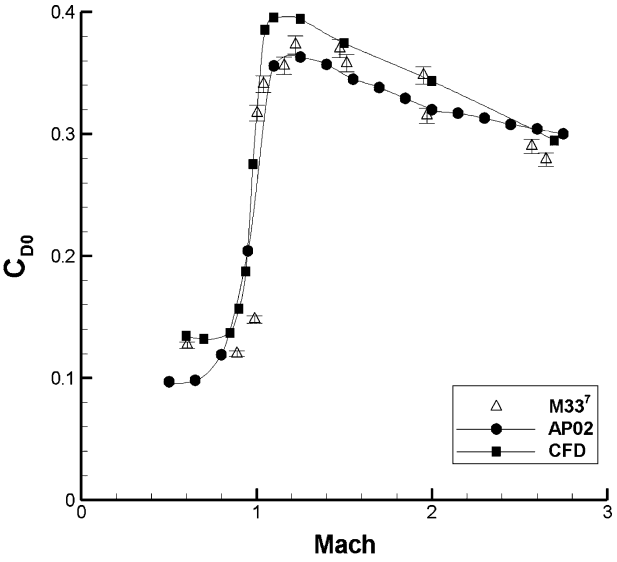

Fig. 11 Zero-yaw drag coefficient vs Mach number.

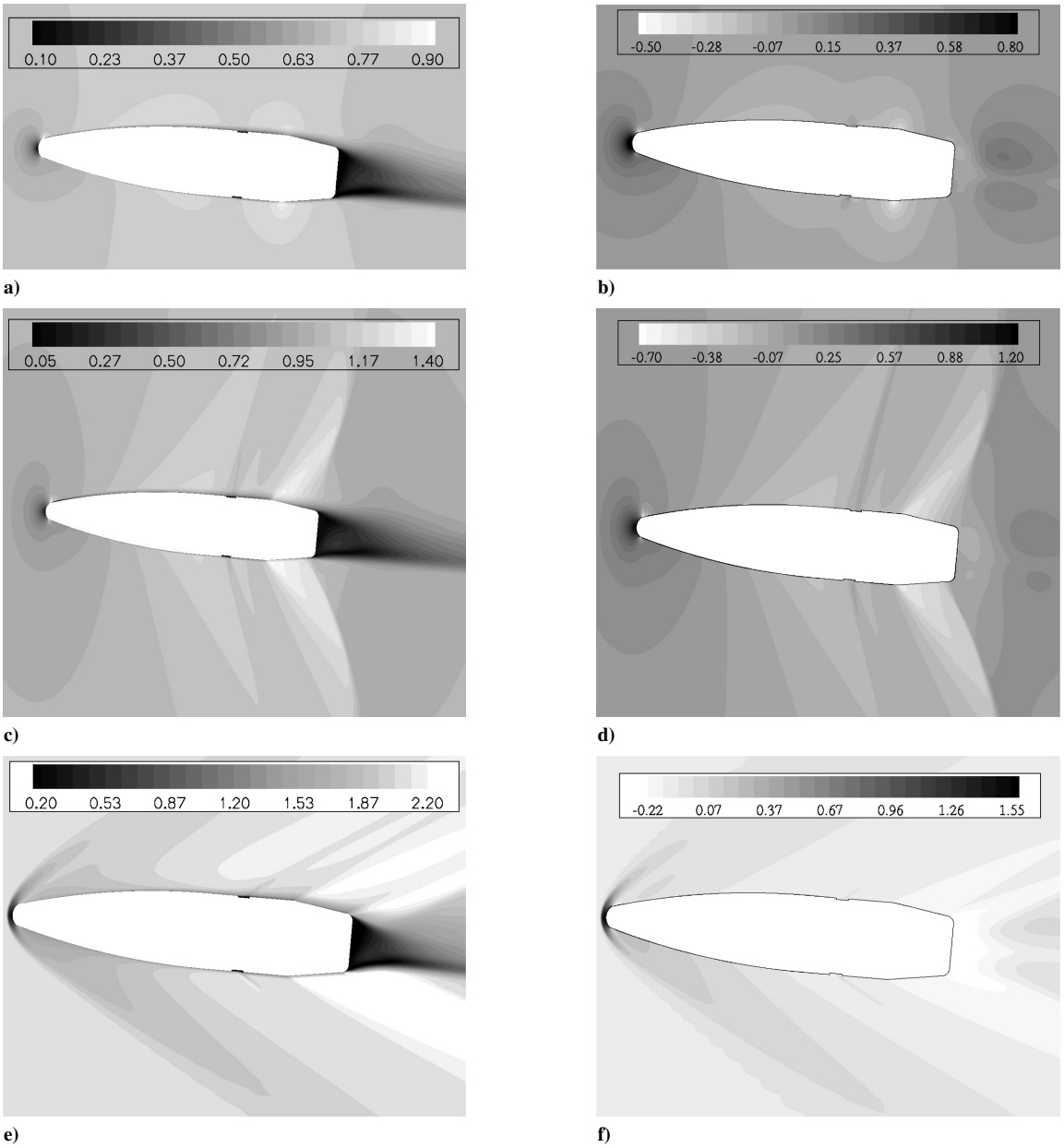

Fig. 10 Mach number and C_p contours on vertical symmetry plane for a,b) $M = 0.70$, c,d) $M = 0.98$, and e,f) $M = 2.0$ at $\alpha = 5$ deg.

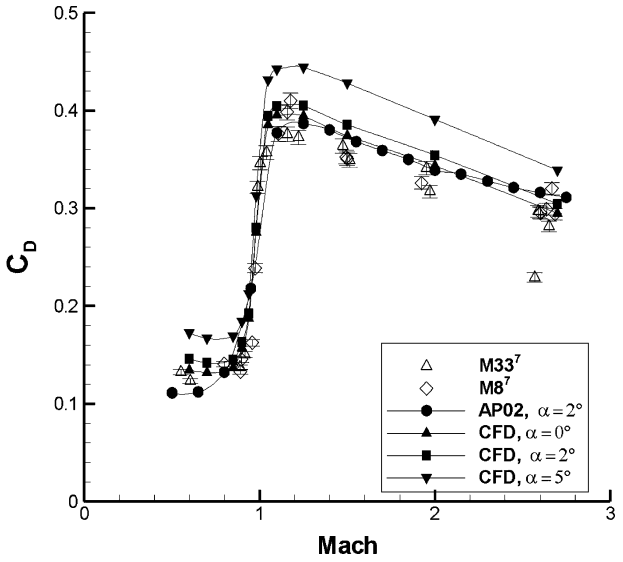

Fig. 12 Drag coefficient vs Mach number (predicted values at α indicated).

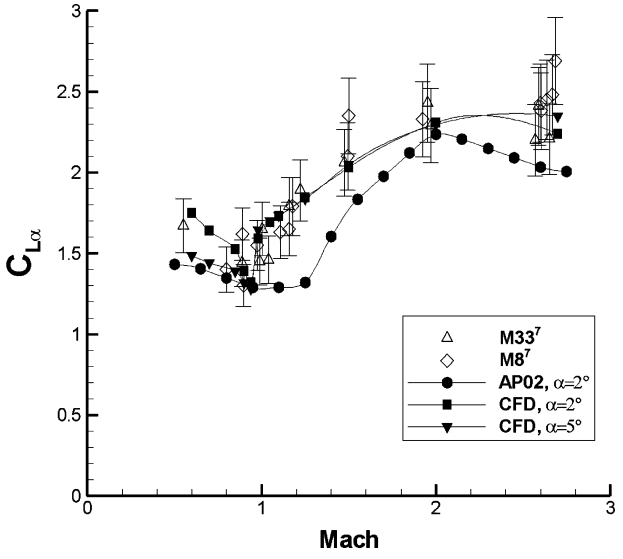

Fig. 13 Lift-force-coefficient derivative vs Mach number.

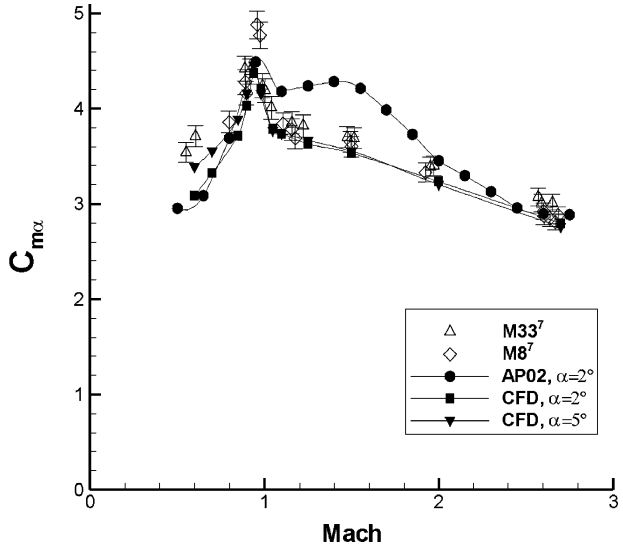

Fig. 14 Overturning moment coefficient derivative vs Mach number.

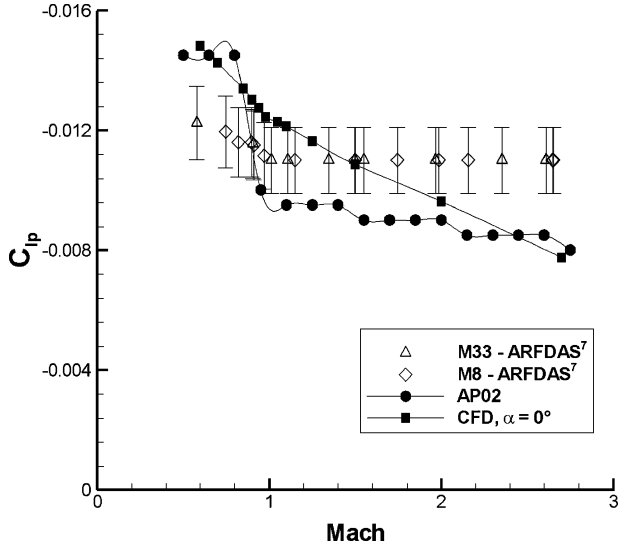

Fig. 15 Roll damping moment coefficient vs Mach number.

nonlinear increase in C_D with angle of attack even at these small angles of attack.

$C_{L\alpha}$ (Fig. 13) and $C_{M\alpha}$ (Fig. 14) were also directly compared to experimental data with much success. The CFD correctly predicted the critical behavior of the pitching moment in the transonic regime, which the semi-empirical code is not able to capture. Both the trends of the data as well as the values were in good agreement. Although $C_{L\alpha}$ and $C_{M\alpha}$ are often calculated these days, the critical behavior in the transonic regime has not always been easy to capture. Earlier CFD research[17] also showed excellent agreement to experimental data, but was more limited in scope. The CFD shows a variation in $C_{L\alpha}$ with angle of attack for $M \leq 0.85$ and at Mach 2.0, although their the variation with angle of attack for $C_{M\alpha}$ occurs only for $M \leq 0.85$. This indicates that there are likely nonlinear variations in $C_{L\alpha}$ and $C_{M\alpha}$ at these Mach numbers. A greater range of angle of attack is necessary in order to determine if indeed a nonlinearity exists.

The dynamic derivative coefficients C_{lp} and $C_{\mathrm{Mp}\alpha}$ were computed as part of the current study. The M33 and M8 data have recently been rereduced using the newer range reduction software, ARFDAS.[18] The dynamic derivative coefficients obtained using multiple data fit option of ARFDAS are compared. The data obtained from the ARFDAS reduction are so indicated.

C_{lp} does not seem to be much affected by angle of attack, as the value of this coefficient varies by only a few percent over the angles of attack investigated. The C_{lp} predicted by both CFD and the semi-empirical code are of the same magnitude as the experimental results but do not show the same trends with Mach number (Fig. 15). The semi-empirical code predicts a nearly constant C_{lp} for $M \geq 1$, although it is smaller than seen in the range analysis. In the subsonic regime, the semi-empirical code overpredicts the value and completely misses the trend. CFD fares a lot better. In the subsonic regime, CFD has the same trend as the range analysis, but overpredicts C_{lp}. For $M \geq 1$, CFD predicts a linear decrease with Mach number.

The agreement at Mach 1.5 seems to be purely coincidental. However, the trends of the CFD at supersonic Mach numbers (Mach 1.5, 2.0, 2.7) do agree with those calculated from a PNS flow solver[8] suggesting that the presence of engraving causes the roll damping to asymptote at supersonic Mach numbers, while the roll damping would continue to decrease without the grooves present. It is likely that the presence of the engraving has a large influence on the roll damping, and thus CFD would be unable to accurately predict C_{lp} unless engraving is included is the model.

As a range of angle of attack was investigated experimentally, it was important to extrapolate the experimental data to the angle of attack investigated numerically when comparing $C_{\mathrm{Mp}\alpha}$. $C_{\mathrm{Mp}\alpha}$ was plotted vs effective square yaw by McCoy[7] for a given Mach number range for the combined M33 and M8 data. Within each flow regime, these plots show a bicubic variation of Magnus moment (Fig. 16). This means that $C_{\mathrm{Mp}\alpha}$ has a cubic variation with angle of attack

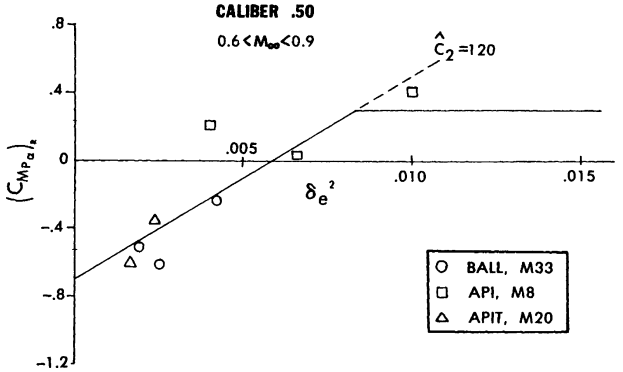

Fig. 16 Magnus moment coefficient derivative vs effective square yaw for $0.6 < M < 0.90$ (Ref. 7).

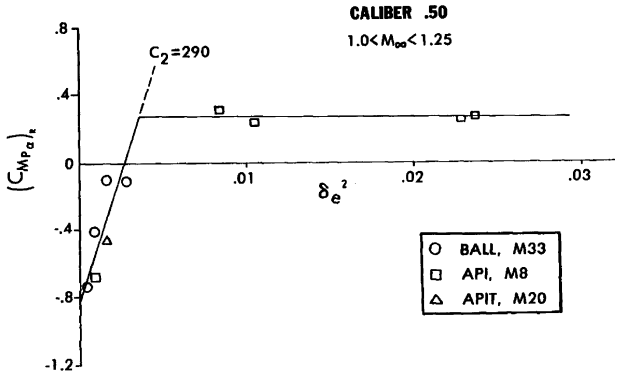

Fig. 17 Magnus moment coefficient derivative vs effective square yaw for $1.0 < M < 1.25$ (Ref. 7).

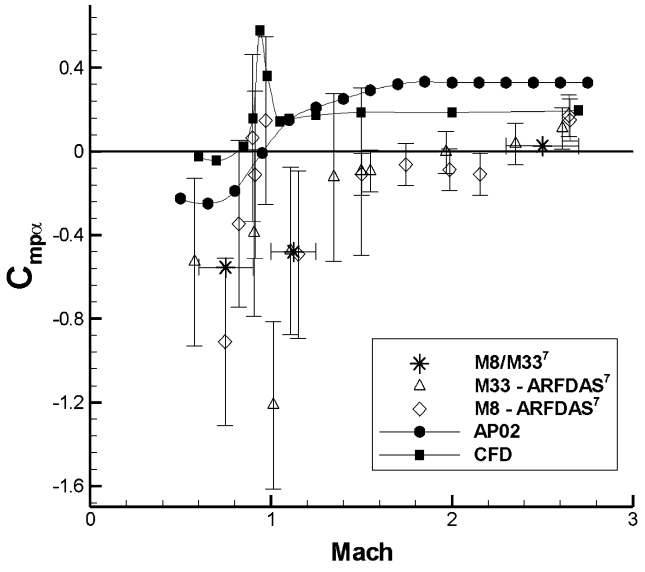

Fig. 18 Magnus moment coefficient derivative vs Mach number for $\alpha = 2$ deg.

at small angle and is linear at high angles of attack. For example, at $\alpha = 2$ deg ($\delta_e^2 = 0.001$), $C_{\mathrm{M}p\alpha}$ has a cubic variation for all Mach numbers investigated. At $\alpha = 5$ deg ($\delta_e^2 = 0.0076$), $C_{\mathrm{M}p\alpha}$ still appears to have a cubic variation for Mach numbers less than 0.90, while it is linear for Mach numbers greater than 1 (Fig. 17). Therefore, because of the way in which $C_{\mathrm{M}p\alpha}$ was calculated for the CFD results (assuming linear variation), Magnus moment coefficient derivatives could be expected to agree better at $\alpha = 5$ deg than at $\alpha = 2$ deg. The exception at $\alpha = 5$ deg would be for Mach numbers less than approximately 0.9, as $C_{\mathrm{M}p\alpha}$ is likely to still have a cubic term.

At $\alpha = 2$ deg (Fig. 18), neither the semi-empirical code nor the CFD does very well in predicting $C_{\mathrm{M}p_\alpha}$. In the supersonic regime,

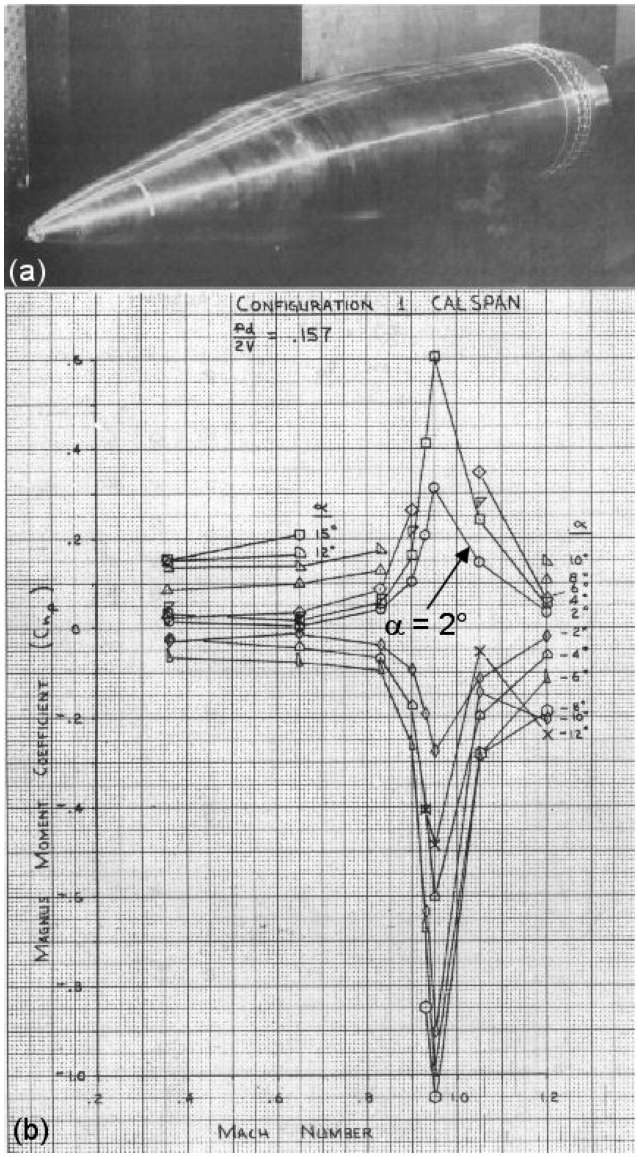

Fig. 19 The 155-mm artillery round a) photo and b) Magnus moment coefficient vs Mach number for various angles of attack.[19]

the range analysis show that $C_{\mathrm{M}p\alpha}$ remains approximately constant. Both the CFD and semi-empirical code predict this supersonic trend, although the value is large. In the subsonic regime, both predictive methods expect negative coefficients, which is confirmed by the range data. The magnitude of the coefficients, however, is in question. The error in the range data is quite large, as well as scattered, so that it is unclear as to what the trends actually are. In the transonic regime, there is no agreement between the predicted values and the range data. Even agreement between the different experimental data sets is not very good in this flow regime.

The differences in experimental data in the subsonic and transonic regimes can most probably be attributed to the differences that occur in the engraving of the rounds as the rounds are made of different materials. Therefore, it is also possible that in addition to the nonlinearity at $\alpha = 2$ deg the lack of engraving on the CFD model could contribute to the disagreement with the experimental results. In fact, if one compares the shape of the Magnus moment coefficient curve obtained experimentally for the 155-mm artillery round[19] at $\alpha = 2$ deg (Fig. 19, as indicated) to that obtained numerically for the 0.50-cal. round at $\alpha = 2$ deg (Fig. 18), they are nearly identical. Perhaps a future CFD analysis can be performed on an artillery round in order to determine just how much effect the engraving has.

At $\alpha = 5$ deg, the data trends in the CFD solution, the semi-empirical solution, and experimental analysis appear to agree rather well (Fig. 20). This could be expected as the $C_{\mathrm{M}p\alpha}$ is no longer

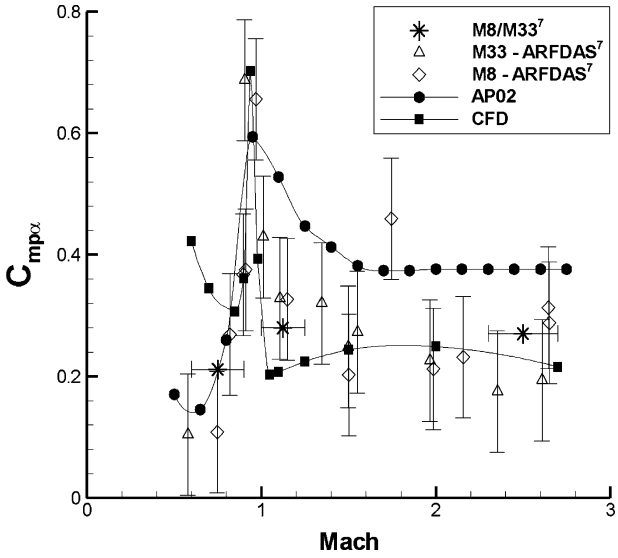

Fig. 20 Magnus moment coefficient derivative vs Mach number for $\alpha = 5$ deg.

nonlinear at this angle of attack for most Mach numbers. CFD agreement with the experimental data in the supersonic regime is quite good, accurately predicting both trend and magnitude. The semi-empirical code does not do as well as the CFD in this regime because, although the data trend is correct, the actual coefficient values are not.

The CFD accurately predicted the critical behavior in the transonic regime. However, as Mach 1 is approached, CFD appears to underpredict $C_{\mathrm{Mp}\alpha}$, although if one considers the error level of the experimental, CFD does alright. The semi-empirical code underpredicted the peak value in the transonic regime and did not capture the critical behavior very well.

In the subsonic regime, the semi-empirical code does a better job predicting the magnitude of $C_{\mathrm{Mp}\alpha}$ than the CFD. CFD significantly overpredicts $C_{\mathrm{Mp}\alpha}$ in the subsonic regime although the trend is similar to that of the semi-empirical prediction. The overprediction at the subsonic Mach numbers might be caused, in part, by the continuing nonlinearity of $C_{\mathrm{Mp}\alpha}$ at the higher angle of attack (Fig. 16). As both the $\alpha = 2$ and 5 deg subsonic cases were significantly overpredicted by the CFD, it is also possible that the assumptions made in the CFD are not appropriate at these Mach number in order to accurately predict $C_{\mathrm{Mp}\alpha}$. With the current assumptions, CFD can be used to predict $C_{\mathrm{Mp}\alpha}$ in the transonic and supersonic regimes for angles of attack thought to be in the linear regime of this coefficient with bicubic variation.

Summary

A computational study has been undertaken to predict the aerodynamic coefficients of a standard spinning projectile using a modern unstructured Navier–Stokes flow solver. Numerical results have been obtained for a wide range of Mach numbers covering the subsonic, transonic, and supersonic flight regimes. Effects of 0-, 2-, and 5-deg angles of attack have been investigated. There is a significant amount of experimental range data available for comparison in these cases. A comparison of aerodynamic coefficients obtained from CFD, a semi-empirical code (AP02), and aeroballistic range data was completed. This comparison showed that CFD modeling a smooth projectile body is able to provide reasonably good prediction of static aerodynamic coefficients for a rifled projectile. The drag coefficient at $\alpha = 2$ deg, the lift-force-coefficient derivative, and overturning moment coefficient derivative are well matched. The dynamic derivative coefficients for spinning projectiles are more sensitive to the rifling, and the agreement is not as good. The roll-damping moment cannot be accurately predicted without modeling the rifling, though CFD predictions are no worse than the semi-empirical predictions. Discrepancies in Magnus moment occur in the subsonic regime at all angles of attack and for all Mach numbers at $\alpha = 2$ deg. These discrepancies are possibly a result of a known nonlinearity in Magnus moment coefficient derivatives. CFD on a rifled projectile ought to be investigated with this software as well as other software to more fully understand the effects of the engraving as well as the extent to which the software can be utilized. Therefore, although one should question the roll-damping moment obtained from the CFD if rifling is neglected and Magnus moment coefficients must be carefully analyzed to determine if nonlinearities are present, the overall results can be utilized for design purposes.

Acknowledgments

This work was supported by a grant of computer time from the Department of Defense High Performance Computing Major Shared Resource Center at the U.S. Army Research Laboratory. The author thanks J. Sahu for discussions and assistance in using the software and analyzing the data. The author thanks ArrowTech Associates for extracting the original 1988 raw Aerodynamic Range free-flight data on the 50-cal. projectile from the archives and analyzing the M33 and M8 data using ARFDAS. The author also thanks P. Weinacht and P. Plostins for their many discussions during completion of the data comparison, especially the dynamic derivatives.

References

[1]Sturek, W. B., and Schiff, L. B., "Computations of the Magnus Effect for Slender Bodies in Supersonic Flow," *AIAA Journal*, Vol. 20, No. 12, 1982, pp. 1724–1731.

[2]Nietubicz, C. J., Sturek, W. B., and Heavey, K. R., "Computations of Projectile Magnus Effect at Transonic Velocities," U.S. Army Ballistic Research Lab., ARBRL-TR-02515, Aberdeen Proving Ground, MD, Aug. 1983.

[3]Sahu, J., "Transonic Navier–Stokes Computations for a Spinning Body of Revolution," U.S. Army Ballistic Research Lab., BRL-TR-3265, Aberdeen Proving Ground, MD, Sept. 1991.

[4]Sylvester, M. A., and Braun, W. F., "The Influence of Helical Serrations and Bullet Engraving on the Aerodynamic and Stability Properties of a Body of Revolution with Spin," U.S. Army Ballistic Research Lab., BRL Rept. 1514, Aberdeen Proving Ground, MD, Nov. 1970.

[5]Sylvester, M. A., "Wind Tunnel Magnus Tests of Cylindrical and Boattail Army-Navy Spinner Projectiles with Smooth Surface and 20 mm Equivalent Engraving (Rifling Grooves)," U.S. Army Ballistic Research Lab., BRL-1758, Aberdeen Proving Ground, MD, Feb. 1975.

[6]Hitchcock, H. P., "Aerodynamic Data for Spinning Projectiles," U.S. Army Ballistic Research Lab., BRL Rept. 620, Aberdeen Proving Ground, MD, Oct. 1947.

[7]McCoy, R. L., "The Aerodynamic Characteristics of .50 Ball, M33, API, M8, and APIT, M20 Ammunition," U.S. Army Ballistic Research Lab., BRL-MR-3810, Aberdeen Proving Ground, MD, Jan. 1990.

[8]Guidos, B. J., and Chung, S. K., "Computational Flight Design of .50 Caliber Limited Range Training Ammunition," U.S. Army Research Lab., ARL-TR-662, Aberdeen Proving Ground, MD, Jan. 1995.

[9]Sahu, J., Heavey, K. R., and Edge, H. L., "Numerical Computations of Supersonic Flow Over Elliptical Projectiles," U.S. Army Research Lab., ARL-TR-2589, Aberdeen Proving Ground, MD, Dec. 2001.

[10]*Gridgen User's Manual*, Pointwise, Inc., Bedford, TX, 1998.

[11]*Fluent 5.0 Users Guide*, Vol. 2, Fluent, Inc., Lebanon, NH, 1998.

[12]*CFD++ User's Manual*, Metacomp Technologies, Westlake Village, CA, 2000.

[13]Goldberg, U. C., Peroomian, O., and Chakravarthy, S., "A Wall-Distance-Free K-E Model with Enhanced Near-Wall Treatment," *Journal of Fluids Engineering*, Vol. 120, Sept. 1998, pp. 457–462.

[14]Moore, F. G., and Hymer, T. C., "The 2002 Version of the Aeroprediction Code: Part II—User's Guide," U.S. Naval Surface Warfare Center, Dahlgren Div., NSWCDD/TR-02/34, Dahlgren, VA, May 200.

[15]Murphy, C. H., "Free Flight Motion of Symmetric Missiles," U.S. Army Ballistic Research Lab., BRL Rept. 1193, Aberdeen Proving Ground, MD, March 1963.

[16]*ARFDAS Technical Manual*, Arrow Tech Associates, South Burlington, VT, 2001.

[17]Sahu, J., "Numerical Computations of Transonic Critical Aerodynamic Behavior," *AIAA Journal*, Vol. 28, No. 5, 1990, pp. 807–816.

[18]*ARFDAS 4.11 User's Guide*, Arrow Tech Associates, South Burlington, VT, 1997.

[19]Kline, R. W., and Hoffman, T. D., "Static and Magnus Aerodynamic Characteristics of the 155-mm M483 Projectile and Its Modifications," Feltman Research Lab., TR-4942, Picatinny Arsenal, Dover, NJ, Aug. 1976.

R. Cummings
Associate Editor